Numerical aspects of polymer flooding

Trine S. Mykkeltvedt* Ivar Aavatsmark Knut-Andreas Lie

Abstract

In this work we discuss the application of modern high-resolution schemes to a hyperbolic system that models polymer flooding. Polymer flooding is a difficult process to model, especially since the dynamics of the flow lead to concentration fronts that are not self-sharpening. Because the water viscosity is strongly affected by the polymer concentration, it is crucial to capture polymer fronts accurately to resolve the nonlinear displacement mechanism correctly and its efficiency for oil enhanced recovery.

The main objective of this work is to compare different first- and higher-order methods in terms of how the discontinuities are treated. Especially, different initial conditions and the inclusion of adsorption and permeability reduction can change not only the solution, but also the behavior of the different numerical methods. We find some numerical artifacts and we investigate of how suitable different numerical methods are for different polymer flooding situations.

Introduction

A widely used Enhanced Oil Recovery (EOR) strategy is polymer flooding. Polymer is a water solute added to the water to increase its viscosity. This increase in viscosity enhances the water ability to push oil through the rock because of a more favorable mobility ratio between the injected and displaced fluids, Lake (1989).

During polymer flooding through a reservoir there is usually adsorption of polymer molecules onto the reservoir rock surface. Adsorption decreases the polymer concentration and consequently the viscosity in the water flood. Thus, adsorption represents a net reduction in the polymer slug. One effect of polymer adsorption is that there can be a pure water bank at the leading edge of the slug. The adsorption process is complex and depends on many factors: polymer concentration, polymer type, pH, salinity, ionic strength, and reservoir heterogeneity. This and consequences of the adsorption for the polymer flooding has been studied in the literature, see e.g., Dang et al. (2011). Adsorption onto the pore walls shrinks the pore volumes. Thus, the permeability of the rock can be reduced. Studies as e.g., Ogunberu and Asghari (2005) indicate a selective action of the polymer with a significant reduction in the relative permeability to water with respect to relative permeability to oil. Another effect of polymer flooding is that smaller portions of the pore space will not allow polymer molecules to enter because of their size. Thus, a portion of the total pore space is inaccessible to the polymer and the polymer flow is accelerated.

The two-phase flow of oil and water with polymer can be modeled using a pair of non-linear hyperbolic conservation laws. In this system, the polymer bank is described by linear waves that, unlike water fronts, are not self-sharpening. Resolving these waves is essential to accurately predict the enhanced oil recovery effect of a polymer flood. This can be a challenge using standard low-order methods, whose large numerical diffusion will tend to smooth the polymer bank and hence fail to accurately resolve the EOR effect. To overcome this challenge, one can use a very fine grid or apply high-resolution schemes. In this work, we will discuss the latter. High-resolution schemes are in general at least second-order accurate on smooth solutions and yet give well resolved, non-oscillatory discontinuities for scalar-equations.

In this work, we discuss the performance of first- and higher- order schemes for different flow situations. In particular, we include the effect of adsorption and permeability reduction in the polymer flood model and study the flow of this system through numerical examples in one dimension. Through numerous numerical experiments we discuss different phenomena that occur for different flow situations for different numerical schemes. Also, we discuss the applicability of different Riemann solvers for this system.

This paper is structured as follows; first, the hyperbolic conservation laws used to represent the polymer flooding is given. Next, the numerical framework is presented before we give the concrete model setup and parameters used in the numerical experiments performed. These experiments are presented, and different findings are discussed before we conclude and summarize the paper.

Mathematical Model

When polymer is added to the water the reservoir fluid consists of three components: oil, water and polymer. We assume that the oil forms its own liquid phase and that water and polymer coexist in the aqueous phase. Polymer flooding is thus a two-phase immiscible system and can be modeled by an extension of the classical Buckley-Leverett model for two-phase flow. This extension was first presented in Pope (1980).

Let ρ_α, s_α, and $\mathbf{u}_\alpha$ denote the density, saturation, and velocity of phase α. Phase $\alpha = n$ represents the non-wetting oil phase and phase $\alpha = w$ represents the aqueous phase. Furthermore, ϕ represents

porosity. The mass-conservation equations for the three components oil, water, and polymer reed

$$(\phi\rho_n s_n)_t + \nabla\cdot(\rho_n \mathbf{u}_n) = 0, \tag{1a}$$
$$(\phi\rho_w s_w)_t + \nabla\cdot(\rho_w \mathbf{u}_w) = 0, \tag{1b}$$
$$(\phi\rho_w s_w c + (1-\phi_r)\rho_r \bar{a}(c))_t + \nabla\cdot(\rho_w c \mathbf{u}_{wp}) = 0, \tag{1c}$$

where c is the polymer concentration, ρ_r the reference rock density, and ϕ_r the reference porosity. In (1c), the term $\bar{a}(c)$ represents the amount of polymer adsorbed by the rock, only dependent of the polymer concentration c. Also, $\mathbf{u}_{wp}$ is the velocity of water containing polymer. We assume that the reservoir rock is homogeneous, thus the porosity and the total permeability of the rock are constant. Also, we assume that the phases are incompressible, that is ρ_α is constant. Thus, Equations (1a-1c) reduce to

$$\phi\,(s_n)_t + \nabla\cdot\mathbf{u}_n = 0, \tag{2a}$$
$$\phi\,(s_w)_t + \nabla\cdot\mathbf{u}_w = 0, \tag{2b}$$
$$\phi\left(s_w c + \frac{1-\phi_r}{\phi}\frac{\rho_r}{\rho_w}\bar{a}(c)\right)_t + \nabla\cdot(c\mathbf{u}_{wp}) = 0. \tag{2c}$$

The phase velocities are given by Darcy's law

$$\mathbf{u}_\alpha = -\lambda_\alpha\left(\nabla p_\alpha - \rho_\alpha \mathbf{g}\right), \tag{3}$$

where the mobilities are

$$\lambda_n = \mathbf{k}\frac{k_{rn}(s_w)}{\mu_n}, \qquad \text{and} \qquad \lambda_w = \mathbf{k}\frac{k_{rw}(s_w)}{\mu_w(c)R(c)}. \tag{4}$$

In (4) $\mathbf{k}$ is the absolute permeability, $k_{r\alpha}(s_w)$ the relative permeability of phase α, μ_α the phase viscosity and $R(c)$ models the reduction in permeability of the rock to the water phase due to adsorption. Here we have assumed that the viscosity of oil is constant, and that the viscosity of the aqueous phase increases as the concentration of polymer increases. We assume that polymer does not affect the pressure and density and that the relative permeability does not depend on mixing. Thus the velocity $\mathbf{u}_{wp}$ is given by

$$\mathbf{u}_{wp} = -\lambda_{wp}\left(\nabla p_w - \rho_w \mathbf{g}\right),$$
$$\text{where} \qquad \lambda_{wp} = \mathbf{k}\frac{k_{rw}(s_w)}{\mu_p(c)R(c)}.$$

Hence, we have that

$$\mathbf{u}_{wp} = m(c)\mathbf{u}_w,$$
$$\text{where} \qquad m(c) = \frac{\mu_w(c)}{\mu_p(c)},$$

and $m(c)$ is called the polymer mobility factor. In this work, we assume that $m(c) = 1$. That is, we assume that the polymer is fully mixed in water. More on a formulation including the degree of mixing can be found in Todd and Longstaff (1972).

To simplify notation, let $s = s_w$ and let the total velocity be given by $\mathbf{u} = \mathbf{u}_w + \mathbf{u}_n$. We subtract the phase velocities given by (3) and get an isolated expression for $\mathbf{u}_w$,

$$\mathbf{u}_w = \frac{\lambda_w}{\lambda_w + \lambda_n}\left(\mathbf{u} + \left(\nabla p_c + (\rho_w - \rho_n)\mathbf{g}\right)\lambda_n\right),$$

where $p_c = p_n - p_w$ is the capillary pressure. For simplicity we neglect the capillary pressure p_c and set the porosity $\phi = 1$. Then, the mass-conservation equation for the aqueous phase (2b) can be written as

$$s_t + \nabla \cdot \mathbf{f}(s,c) = 0, \tag{5}$$

$$\text{where} \qquad \mathbf{f}(s,c) = \frac{\lambda_w}{\lambda_w + \lambda_n}\left[\mathbf{u} + \lambda_n (\rho_w - \rho_n)\,\mathbf{g}\right], \tag{6}$$

and $\mathbf{f}(s,c)$ is called the flux function of the system. Similarly, if we let $a(c) = \frac{\rho_r}{\rho_w}\bar{a}(c)$, the mass-conservation equation for the polymer component (2c) can be written as

$$(sc + a(c))_t + \nabla \cdot (c\mathbf{f}(s,c)) = 0. \tag{7}$$

From now on we consider the hyperbolic system consisting of (5) and (7) in one dimension,

$$s_t + f(s,c)_x = 0, \tag{8a}$$

$$(sc + a(c))_t + (cf(s,c))_x = 0, \tag{8b}$$

where the flux function $f(s,c)$ is given by

$$f(s,c) = \frac{\lambda_w}{\lambda_w + \lambda_n}\left[u \pm \lambda_n(\rho_w - \rho_n)g\right], \tag{9}$$

and the sign in front of $\lambda_n(\rho_w - \rho_n)g$ depends on what type of flow we are considering (e.g., up and down dip flow).

The pair of equations (8a-8b) is the conservation form of the polymer flood model. This can be written in the nonconservative form as

$$\begin{aligned} s_t + f_s(s,c)s_x + f_c(s,c)c_x &= 0, \\ (s + a'(c))c_t + f(s,c)c_x &= 0, \end{aligned}$$

which on matrix form is

$$\begin{aligned} &U_t + AU_x = 0, \\ &\text{where} \qquad U = \begin{bmatrix} s \\ c \end{bmatrix} \qquad \text{and} \qquad A = \begin{bmatrix} f_s(s,c) & f_c(s,c) \\ 0 & \frac{f(s,c)}{s + a'(c)} \end{bmatrix}. \end{aligned}$$

The eigenvalues λ^p of the Jacobian matrix A are

$$\lambda^s(s,c) = f_s(s,c), \qquad \text{and} \qquad \lambda^c(s,c) = \frac{f(s,c)}{s + a'(c)}.$$

The system (8a-8b) can have equal eigenvalues ($\lambda^s = \lambda^c$), and hence this is a system of non-strictly hyperbolic conservation laws.

Polymer is often injected in slugs, and we need to consider discontinuous initial data. The system (8a-8b) with the initial conditions

$$\begin{aligned} s(x,0) &= \begin{cases} s^L, & \text{if } x < 0, \\ s^R, & \text{if } x \geq 0, \end{cases} \\ c(x,0) &= \begin{cases} c^L, & \text{if } x < 0, \\ c^R, & \text{if } x \geq 0, \end{cases} \end{aligned} \tag{10}$$

is a Riemann problem. This problem (with the adsorption $a(c) = 0$) was first analyzed by Isaacson (1989); Temple (1982), who neglected gravity and obtained a system in which the flux function $f(s,c)$

is monotone. The extension of this model with $a(c) \neq 0$ was analyzed and a unique global solution of this Riemann problem was derived by Johansen and Winther (1988). When gravity effects are included, the flux function can be non-monotone and thus the eigenvalues λ^p can change sign and the exact solution of the Riemann problem is more difficult to construct. For details on the different wave-compositions and solution of the Riemann problem in the general case where gravity effects are included and the flux function can be non-monotone, see e.g., Sudarshan Kumar et al. (2013).

The solution of the general Riemann problem consist of what in the literature is referred to as s-waves and c-waves. An s-wave is any composition of simple rarefaction or shock (or contact discontinuity) waves across which s changes continuously and discontinuously, respectively. A c-wave is a simple c-rarefaction wave or a c-shock (or contact discontinuity) wave such that s and c changes for which $\frac{f(s,c)}{s+a'(c)}$ remain constant and

$$\frac{f(s^L,c^L)}{s^L+a'(c^L)} = \frac{f(s^R,c^R)}{s^R+a'(c^R)}.$$

The detailed theory on the solution of the Riemann problem will not be discussed further in this work.

Numerical Model

In this section, we present the numerical approach we have used to model the polymer flooding (8a-8b). For simplicity we let $(x_i,t^n) := (i\Delta x, n\Delta t)$ be a uniform grid. The approach is presented for a general system of conservation laws,

$$Q_t + H(Q)_x = 0, \tag{11}$$

and follows classical theory presented in e.g., LeVeque (1992). The system (8a-8b) on the general form (11) corresponds to

$$Q = \begin{bmatrix} s \\ sc+a(c) \end{bmatrix}, \qquad H(Q) = \begin{bmatrix} f(s,c) \\ cf(s,c) \end{bmatrix}.$$

To simplify our transition from the classical first-order to a higher-order numerical scheme we use the semi-discrete finite volume framework presented in e.g., Hagen et al. (2007). That is, we reduce the system of partial differential equations to a system of ordinary differential equations, to which we then apply an ODE solver. This is done to be able to decouple the issues of spatial and temporal accuracy and is called the method of lines. First, we start with the cell-average $Q_i(t)$ over each grid-cell,

$$Q_i(t) = \frac{1}{\Delta x}\int_{x_{i-1/2}}^{x_{i+1/2}} Q(\xi,t)\, d\xi, \tag{12}$$

and impose the integral form of (11) on the
cell $(x_{i-1/2}, x_{i+1/2})$

$$\frac{d}{dt}\int_{x_{i-1/2}}^{x_{i+1/2}} Q(\xi,t)\, d\xi = H(Q(x_{i-1/2},t)) - H(Q(x_{i+1/2},t)). \tag{13}$$

By combining (12) and (13) we arrive at a system of ODEs

$$\frac{d}{dt}Q_i(t) = -\frac{1}{\Delta x}\left(H_{i+1/2}(t) - H_{i-1/2}(t)\right), \tag{14}$$

and the fluxes across the cell-boundaries are given by

$$H_{i+1/2} = H(Q^L_{i+1/2}, Q^R_{i+1/2}),$$

where $Q^L_{i+1/2}$ and $Q^R_{i+1/2}$ are the reconstructed point values of Q to the left and to the right of the corresponding cell face. For now, we assumed that

$$Q^L_{i+1/2} = Q_i, \qquad Q^R_{i+1/2} = Q_{i+1}, \tag{15}$$

which is referred to as the constant reconstruction. How to approximate the fluxes $H_{i\pm1/2}$ has been discussed in the literature for decades and the flux-approximations used in this work will be presented shortly. The time integration of the ODE (14) is for a first-order method discretized with forward Euler.

Returning to the ODE (14) for the polymer system (8a-8b), this would read

$$\frac{d}{dt}\begin{bmatrix} s_i \\ s_i c_i + a(c_i) \end{bmatrix} = -\frac{1}{\Delta x}\begin{bmatrix} F_{i+1/2}(t) - F_{i-1/2}(t) \\ G_{i+1/2}(t) - G_{i-1/2}(t) \end{bmatrix}, \tag{16}$$

where the flux $F_{i\pm1/2}$ is associated with $f(s,c)$ and $G_{i\pm1/2}$ is associated with $g(s,c) = cf(s,c)$. The updated value for the saturation s_i^{n+1} is found from the first row and used in the second row to approximate the updated value for the polymer concentration c_i^{n+1} using a Newton-Raphson iteration.

Flux approximation

The numerical fluxes $F_{i\pm1/2}$ in (16) can be approximated in a number of ways, and from this we can easily find $G_{i\pm1/2}$. For now, we let $G_{i+1/2}$ in (16) be given by

$$G_{i+1/2} = \begin{cases} c_i^n F_{i+1/2} & \text{if } F_{i+1/2} > 0, \\ c_{i+1}^n F_{i+1/2} & \text{else.} \end{cases}$$

Popular approximations are centered approximations and approximations based on the solution of the associated Riemann problem.

Let the saturation in the cell to the left of the edge $x_{i+1/2}$, s_i^n be denoted s^L and the value in the cell to the right s_{i+1}^n be denoted s^R. Similarly for the polymer concentration, $c^L = c_i^n$ and $c^R = c_{i+1}^n$.

The *Godunov flux approximation* is based on solving the local Riemann problem for the system (8a-8b) in the domain $(x_{i-1/2}, x_{i+1/2}) \times (t^n, t^{n+1})$ with the initial condition

$$(s(x,t^n), c(x,t^n)) = \begin{cases} (s_i^n, c_i^n), & \text{if } x < x_{i+1/2}, \\ (s_{i+1}^n, c_{i+1}^n), & \text{if } x \geq x_{i+1/2}. \end{cases}$$

The Riemann solution is a similarity solution, i.e., a function of $\xi = x/t$ only. The Godunov flux is found by evaluating $F = f(s,c)$ in $x/t = 0$ and denoted by

$$F_{i+1/2} = F^G(s^L, c^L, s^R, c^R),$$

for details see e.g., Johansen and Winther (1988); Sudarshan Kumar et al. (2013).

The *DFLU flux* is an extension of the Godunov scheme for scalar conservation laws that was proposed in Adimurthi et al. (2004) and applied to the polymer system by Sudarshan Kumar et al. (2013). Looking at the flux approximation related to Equation (8a), we take $c(x,t)$ in $f(s,c)$ as a known function that may be discontinuous at the space discretization points. Thus, in (16), the flux $F_{i+1/2}$ for concave flux functions $f(s,c)$ is taken to be

$$\begin{aligned} F_{i+1/2} &= F^{DFLU}(s^L, c^L, s^R, c^R) \\ &= \min\left[f(\min\{s^L, \theta^L\}, c^L), f(\max\{s^R, \theta^R\}, c^R)\right], \end{aligned}$$

where θ^L and θ^R are the maximum values of $f(s^L,c^L)$ and $f(s^R,c^R)$ respectively. Similarly, for convex flux functions $f(s,c)$, the flux $F_{i+1/2}$ is

$$\begin{aligned} F_{i+1/2} &= F^{DFLU}(s^L,c^L,s^R,c^R) \\ &= \max\left[f(\max\{s^L,\theta^L\},c^L), f(\min\{s^R,\theta^R\},c^R)\right], \end{aligned}$$

where θ^L and θ^R are the minimum values of $f(s^L,c^L)$ and $f(s^R,c^R)$ respectively. Note that the Godunov flux approximation requires the solution of the Riemann problem for the system (8a-8b), while the DFLU flux only requires the solution of the Riemann problem of a scalar equation. In Adimurthi et al. (2013); Sudarshan Kumar et al. (2013) it is shown that the DFLU flux is as good as the Godunov flux, and converges faster than other classical schemes that do not exploit the solution of the Riemann problem.

To avoid the difficulty of solving Riemann problems, it is common to use centered flux approximations. Classical schemes of this kind are the Lax-Friedrichs scheme and the FORCE scheme, for details on these see e.g., LeVeque (1992). In Kurganov et al. (2001) a flux approximation called *central-upwind* was introduced. This is a centered approach in which information about the smallest and largest eigenvalue of the Jacobian matrix of the system is used in the flux evaluation. Let

$$a^+ = \max_{s\in\{s^L,s^R\}}(\lambda_M,0) \qquad\qquad a^- = \min_{s\in\{s^L,s^R\}}(\lambda_m,0),$$

where λ_M and λ_m denote the largest and smallest, respectively, eigenvalues of the Jacobian matrix of the system. The values a^+ and a^- are estimates of how far the Riemann fan from the discontinuity (s^L,s^R) extends in the positive and negative direction. The central-upwind flux approximation is given by

$$\begin{aligned} F_{i+1/2} = \; & F^{CU}(s^L,c^L,s^R,c^R) \\ = \; & \frac{a^+ f(s^L,c^L) - a^- f(s^R,c^R)}{a^+ - a^-} \\ & + \frac{a^+ a^-}{a^+ - a^-}(s^R - s^L). \end{aligned}$$

Note that for monotone flux functions this scheme reduces to the standard upwind scheme.

Numerical schemes based on centered flux approximations are in general more diffusive than schemes based on an exact or an approximate Riemann solver. However, for problems for which the Riemann solution is not known, or is too computationally expensive to find, flux approximations like F^{CU} can be the only option available.

Reconstruction

Returning to the general system of ODE (14) the question now is how to reconstruct the point-values of Q from the cell averages. That is, how to interpolate from cell averages to point values Q. To obtain higher-order accuracy, the constant reconstruction (15) must be improved and a high-order piecewise polynomial interpolant $\tilde{Q}$ from the cell-averages is used. The interpolant must be conservative, non-oscillatory and sufficiently accurate. Note that at a discontinuity, we cannot expect to maintain high-order accuracy, but rather minimize the creation of spurious oscillations. Different high-order reconstructions used in this work will be presented below.

From the cell averages Q_i^n, we construct a piecewice linear function of the form

$$Q^L_{i+1/2} = \; Q_i + \frac{1}{2}\delta_i, Q^R_{i+1/2} = \qquad\qquad Q_{i+1} - \frac{1}{2}\delta_i,$$

where δ_i is the slope on the i-th cell. The linear function in the i-th cell is designed in such a way that the value at the cell-center is exactly Q_i. To obtain a second-order accurate method we chose a nonzero

slope in such a way that δ_i approximates Q_x over the i-th grid cell. Which slope to choose depends on how the solution is behaving near the i-th cell using a given slope δ_i. Near a discontinuity it can be favorable to limit the slope, using a value that is smaller in magnitude to avoid oscillations. Methods based on this approach are called *slope-limiter* methods and was first introduced in a series of papers by Van Leer (1974, 1977, 1979).

In this work, we have used two classical slope-limiters from the literature. This includes the *minmod* limiter

$$\delta_i^n = \text{minmod}\left(\theta\frac{U_i^n - U_{i-1}^n}{\Delta x}, \frac{1}{2}\frac{Q_{i+1}^n - Q_{i-1}^n}{\Delta x}, \theta\frac{Q_{i+1}^n - Q_i^n}{\Delta x}\right), \quad \theta \in [1,2], \tag{17}$$

where

$$\text{minmod}(a,b,c) = \begin{cases} \min(a,b,c), & \text{if } a>0,\ b>0, \text{ and } c>0, \\ \max(a,b,c), & \text{if } a<0,\ b<0, \text{ and } c<0, \\ 0, & \text{otherwise,} \end{cases}$$

and the *superbee* limiter introduced by Roe (1985).

$$\delta_i^n = \text{maxmod}\left(\delta_i^{1,n}, \delta_i^{2,n}\right), \tag{18}$$

where

$$\delta_i^{1,n} = \text{minmod}\left(\frac{Q_{i+1}^n - Q_i^n}{\Delta x}, 2\frac{Q_i^n - Q_{i-1}^n}{\Delta x}\right),$$
$$\delta_i^{2,n} = \text{minmod}\left(2\frac{Q_{i+1}^n - Q_i^n}{\Delta x}, \frac{Q_i^n - Q_{i-1}^n}{\Delta x}\right),$$

and

$$\text{maxmod}(a,b) = \begin{cases} a, & \text{if } |a|>|b| \text{ and } ab>0, \\ b, & \text{if } |a|<|b| \text{ and } ab>0, \\ 0, & \text{else.} \end{cases}$$

The superbee limiter does not reduce the slope as much as the minmod limiter near a discontinuity, and can achieve sharper resolution of discontinuities.

Both limiters mentioned fulfill the *total variation diminishing* (TVD) property. In Harten (1983) it is showed that this property ensures that oscillations are not introduced when the limiter is applied to a scalar equation. When TVD limiters are applied to a system of equations, like the polymer system, this property only ensures that oscillations are not introduced in the reconstruction step. However, this does not guarantee an oscillation-free solution overall.

ODE solver

The system of time-dependent ODEs (14) is solved by an ODE solver. For higher-order reconstructions, one can e.g., use the Runge-Kutta methods described in Shu (1988) to preserve high-order accuracy in time without creating oscillations. A second-order TVD Runge-Kutta solver is given by

$$V^{(1)} = Q^n + \Delta t R(Q^n),$$
$$Q^{n+1} = \frac{1}{2}V^{(0)} + \frac{1}{2}\left[V^{(1)} + \Delta t R(V^{(1)})\right],$$

where $R(Q) = \frac{1}{\Delta x}\left[H(Q_{i+1/2},t) - H(Q_{i-1/2},t)\right]$.

Table 1: The different flux function shapes dependent on which flow that are being considered, see Figure 1.

Flow type	u	$f(s,c)$	**Illustration**	**Case**
Horizontal	0.2	$\frac{\lambda_w}{\lambda_w+\lambda_n}u$	Figure 1a	A
Down dip	0.2	$\frac{\lambda_w}{\lambda_w+\lambda_n}[u+\lambda_n(\rho_w-\rho_n)g]$	Figure 1b	B
Down dip	0	$\frac{\lambda_w}{\lambda_w+\lambda_n}[\lambda_n(\rho_w-\rho_n)g]$	Figure 1c	C
Up dip	0.2	$\frac{\lambda_w}{\lambda_w+\lambda_n}[u-\lambda_n(\rho_w-\rho_n)g]$	Figure 1d	D
Up dip	0	$\frac{\lambda_w}{\lambda_w+\lambda_n}[-\lambda_n(\rho_w-\rho_n)g]$	Figure 1e	E

Numerical Experiments

In this section we first introduce the model setup used for the polymer flood model. Next, we show different results from the numerical simulations to emphasize different aspects of the polymer flood modeling.

Model setup

In the flux function $f(s,c)$ in (9) we let

$$\lambda_w(s,c) = \frac{s^2}{(0.5+c)}\frac{1}{R(c)},$$
$$\text{and } \lambda_n(s) = (1-s)^2.$$

Furthermore, we consider different situations in which both the gravity term and the total velocity u are included or neglected. When these are included, we let $u = 0.2$ and $(\rho_w - \rho_n)g = 1$. When gravity is neglected, we are considering horizontal flow and the resulting flux functions $f^L = f(s,c^L)$ and $f^R = f(s,c^R)$ for a constant value of c^L and c^R such that $c^L > c^R$ have the shape shown in Figure 1a. Similarly, if we are considering down dip flow, the gravity term in (9) has positive sign and the possible shapes of the flux functions f^L and f^R are shown in Figure 1b and 1c with $u = 0.2$ and $u = 0$ respectively. If we consider up dip flow, the gravity term in (9) has negative sign and the possible shapes of the flux functions f^L and f^R are shown in Figure 1d and 1e with $u = 0.2$ and $u = 0$ respectively. These five situations are summarized and given a case letter (A-E) in Table 1 below. At constant temperature, an adsorption isotherm gives a relation between the amount of adsorbed polymer and the polymer concentration c. The Langmuir isotherm theory is a favorable tool for modeling the polymer adsorption process Lake (1989). In this work we have used several representations of the adsorption and these are listed in Table 2 and shown in Figure 2.

The permeability reduction can be modeled by applying a residual resistance factor $R(c)$ to the water relative permeability, see e.g., Schlumberger and Geoquest (2005). Note that this factor must be a constant or increasing function. The permeability reductions used in this work are listed in Table 3.

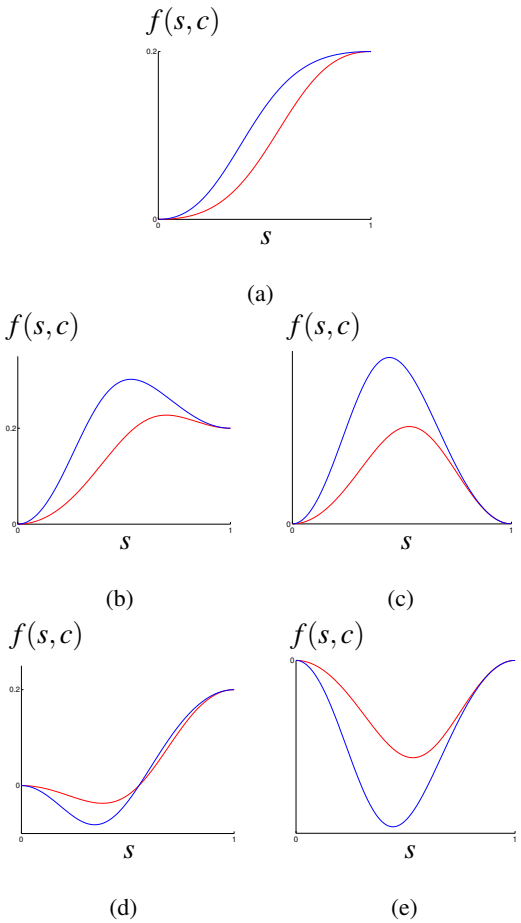

Figure 1: The flux functions associated with the left (red) and right (blue) polymer concentration across a cell edge are considered with the following shapes (here shown for $c^L > c^R$).

Table 2: Different adoption functions $a(c)$ used in this work, numbered with Case 1-5.

	$a(c)$	**Case**
No adsorption	0	1
Linear adsorption	$0.25c$	2
Linear adsorption	c	3
Langmuir adsorption	$\frac{80c}{1+80c}$	4
Linear adsorption	$1+0.5c$	5

Table 3: Different permeability reduction factors used in this work, numbered with Case a-c.

	$R(c)$	**Case**
No permeability reduction	1	a
Constant	1.3	b
Increasing	$1+0.5c^2$	c

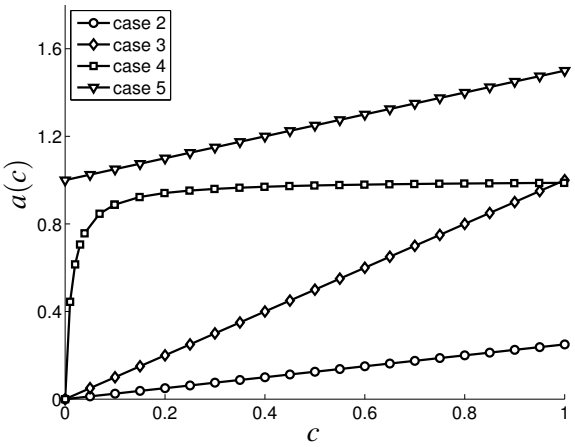

Figure 2: Different choices of the adsorption function $a(c)$.

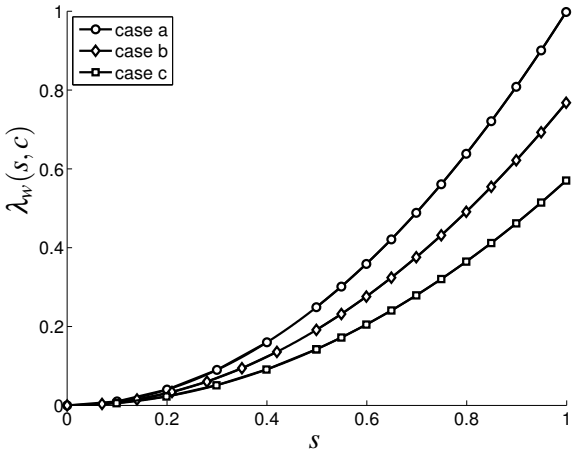

Figure 3: Different $\lambda_w(s,c)$ with $c = 0.5$ for different choices of the permeability reduction $R(c)$.

The different initial conditions used in the numerical examples in this work are

$$(s(x,0),c(x,0)) = \begin{cases} (0.9,0.9) & \text{if } x < 0.5, \\ (0.1,0.3) & \text{if } x \geq 0.5, \end{cases} \tag{19a}$$

$$(s(x,0),c(x,0)) = \begin{cases} (0.9,0.7) & \text{if } x < 0.5, \\ (0.7,0.3) & \text{if } x \geq 0.5, \end{cases} \tag{19b}$$

$$(s(x,0),c(x,0)) = \begin{cases} (0.1,0.9) & \text{if } x < 0.5, \\ (0.9,0.1) & \text{if } x \geq 0.5. \end{cases} \tag{19c}$$

For situations with flux functions of shape A, B, and C, the initial conditions (19a) and (19b) have been used, and for the flux functions of shape D and E, the initial conditions (19b) and (19c) have been used. Boundary conditions are such that

$$\begin{aligned} (s(0,t),c(0,t)) &= (s^L,c^L) \\ \text{and } (s(1,t),c(1,t)) &= (s^R,c^R). \end{aligned}$$

As our a reference solution, we use a converged solution on a fine grid with $\Delta t = \Delta x = \frac{1}{100000}$ found using the constant reconstruction and the Godunov flux approximation.

To illustrate the influence of adding polymer and including adsorption and permeability reduction we show an example of the saturation and concentration front at time $t = 0.5$ for a situation with flux of Case B and initial condition (19a). In the example in Figure 4 we have included a simulation in which no polymer is added (green), one in which polymer is added but adsorption and permeability reduction is neglected (blue), one in which adsorption is of Case 3 and permeability reduction is neglected (red), and one in which adsorption of Case 3 and permeability reduction of Case c is included (black). This simulation illustrates the wanted effect of a slower saturation front when polymer is added. However, when adsorption is included the polymer front itself moves slower and has less effect on the saturation front. When permeability reduction also is included we see that this has little effect on the polymer front, but increases the wanted effect of a slower saturation front. This simulation is shown to give the reader a better understanding of how the flow is affected by the different quantities.

Validity, convergence, and robustness of the numerical schemes

Using the numerical model presented earlier, together with the given model setup, we now show some numerical aspects of the simulation of the polymer flood. First, we study the convergence of the saturation s and the concentration c through the L^1-norm using different reconstructions both for the Godunov, the DFLU, and the central-upwind flux approximation. Let $\bar{U} = (\bar{s},\bar{c})$ denote the reference solution, while $U = (s,c)$ are the numerical approximations found by the specified scheme. The flux shape is taken to be flux B, the initial condition is (19a), the adsorption is the langmuir type in Case 4 and the permeability reduction is neglected. The error development shown in Figure 5 confirms that the DFLU flux performs similar to the Godunov flux. This is good news since the DFLU flux approximation only requires the solution of the Riemann problem for the scalar equation, as we discussed when we introduced these flux approximations. Furthermore, we see that the central-upwind scheme also performs well and similar to the two Riemann solvers.

To emphasize this further, we now show comparisons of simulations with the DFLU and the central-upwind flux approximation. The simulations in Figure 6 are done on a coarse-scale grid, with constant reconstruction. From this figure we see that the simulations done with the two flux-approximations are almost identical. Originally, our hypothesis was that we could find situations where the Riemann solvers would fail because of the complexity of the problem. However, for the model setup we have used in this work, the Riemann solvers performs well. Also, the central-upwind scheme computes almost identical approximations compared to the Riemann solvers, thus we find this scheme applicable to this problem.

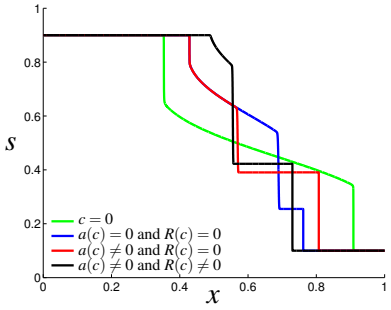

(a) Saturation front at time $t = 0.5$.

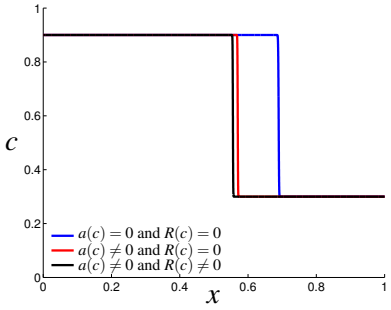

(b) Polymer front at time $t = 0.5$.

Figure 4: Saturation and polymer front for an example with flux B and initial condition (19a). Green: no polymer added, blue: with polymer but no adsorption and permeability reduction, red: adsorption but no permeability reduction, black: adsorption and permeability reduction.

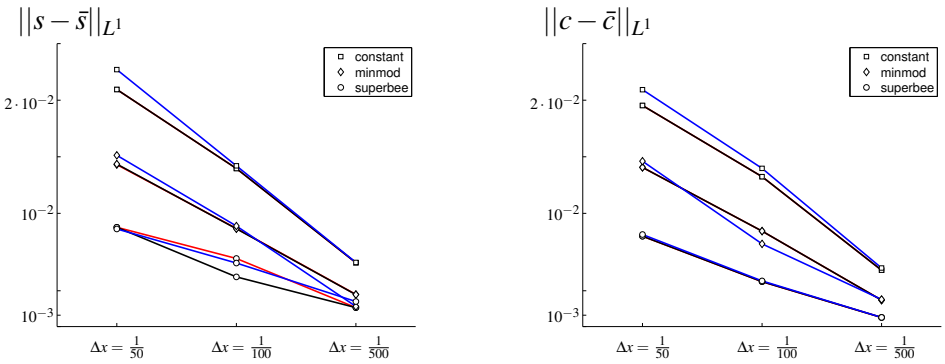

Figure 5: Development of the error $||U - \bar{U}||_{L^1}$ for different flux approximations and reconstructions. These include the Godunov (red), the DFLU (black), and the central-upwind (blue) flux approximations and constant, minmod and superbee reconstructions. Note the development for the DFLU and Godunov flux approximations are almost identical, thus the red curve is hidden under the black.

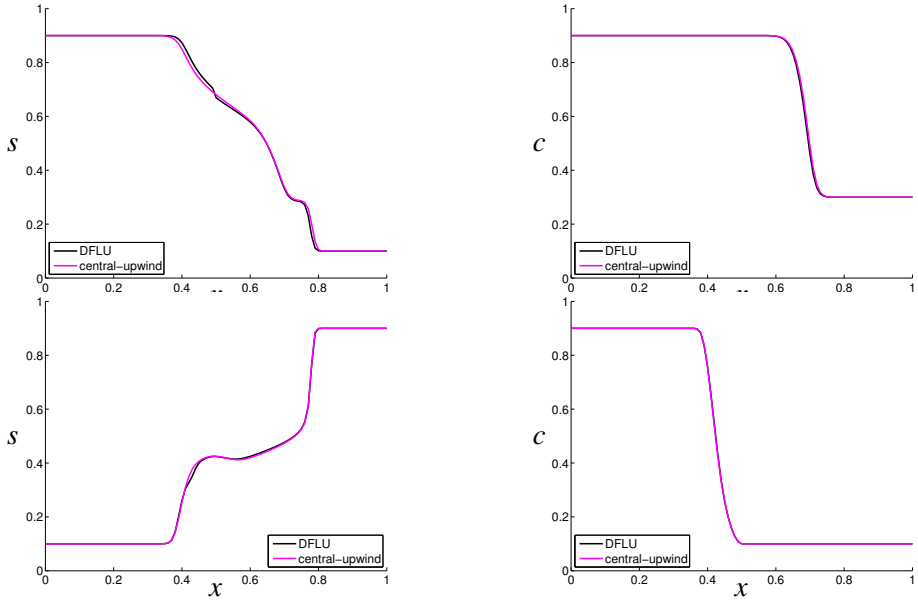

Figure 6: Saturation (left) and polymer (right) front at time $t = 0.5$ computed with the DFLU (black) and the central-upwind (magenta) flux-approximation, using the constant reconstruction. In the top row we have used a flux of shape B and initial condition (19a), and in the bottom row the flux is of shape D and we have used initial condition (19c). The adsorption in both examples is taken to be of Case 4, while permeability reduction is neglected.

From Figure 5 we see that both the minmod and the superbee limiter performs better than the constant reconstruction. Of the two, the superbee slope limiter gives the lowest error. To investigate this trend further, we now study the validity of this slope limiter. First, we compare the saturation and polymer front at time $t = 0.5$ for two examples with flux function of shape B and initial condition (19a) with no permeability reduction and adsorption $a(c) = c$, see Figure 7. The coarse-scale simulations are done with $\Delta x = \Delta t = 1/100$ using constant reconstruction and the higher-order reconstruction with the superbee limiter. For the coarse-scale simulations shown throughout the paper, we have used the central-upwind scheme. The different aspects and phenomenon discussed, are similar for the coarse-scale solutions computed with the Riemann solvers.

Looking on the polymer front in the right column of Figure 7 alone, we see that the superbee limiter does a better job than the constant reconstruction. However, for the case where the adsorption is included (bottom row) we see that the superbee limiter has oscillations in the saturation front. Through numerous of simulations for different flux function shapes, different adsorptions, different permeability reductions, and different initial conditions we have looked for a pattern in when these oscillations occur. Our findings for this phenomenon are summarized in the upper part of Table4.

Another phenomenon of the superbee limiter found through these numerous simulations is the one shown for the saturation front in Figure 8. Here, the propagation speed of the saturation front simulated by the superbee limiter is overestimated. This phenomenon is only found when the flux has the shape C and the initial condition is (19b). Adsorption and permeability reduction does not affect this phenomenon.

When the initial condition (19b) is used with flux function of shape A and B, the saturation front can develop a polymer oil bank. This means that the flooding problems develops an oil bank just ahead of a contact discontinuity, moving at the same speed as the leading edge of a rarefaction. This bank is especially hard to capture for coarse-scale simulations. In Figure 9 we show three situations where the polymer oil bank is simulated with the different reconstructions mentioned earlier. Especially, we see from Figure 9b that a narrow oil bank is particularly hard to capture for the coarse-scale simulations. Not

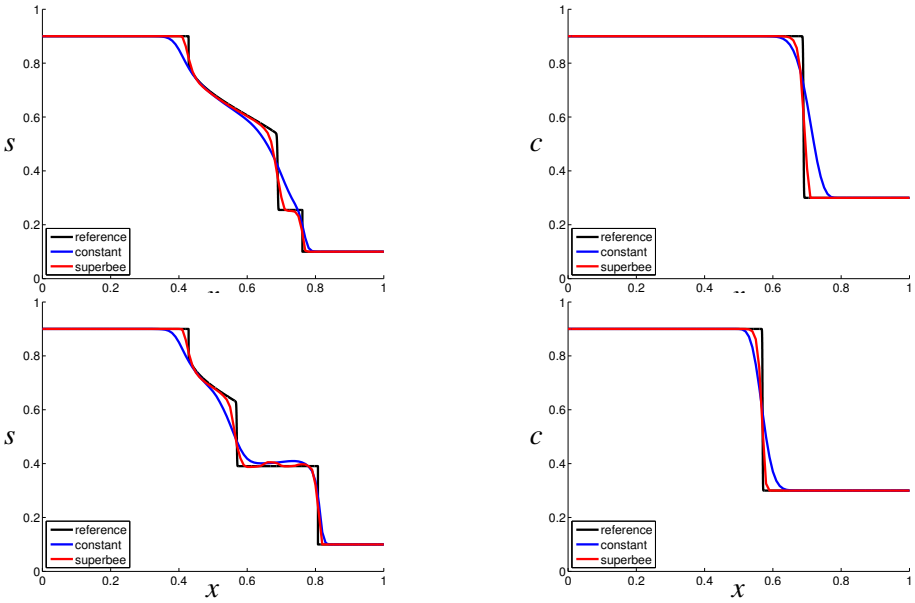

Figure 7: Saturation and polymer front for an example with flux B and initial condition (19a) at time $t = 0.5$. In the top row adsorption is neglected, and in the bottom row adsorption is taken to be $a(c) = c$. Results shown for a reference solution (black) and coarse-scale solutions ($\Delta x = 1/100$) with constant reconstruction (blue) and reconstruction with superbee slope limiter (red).

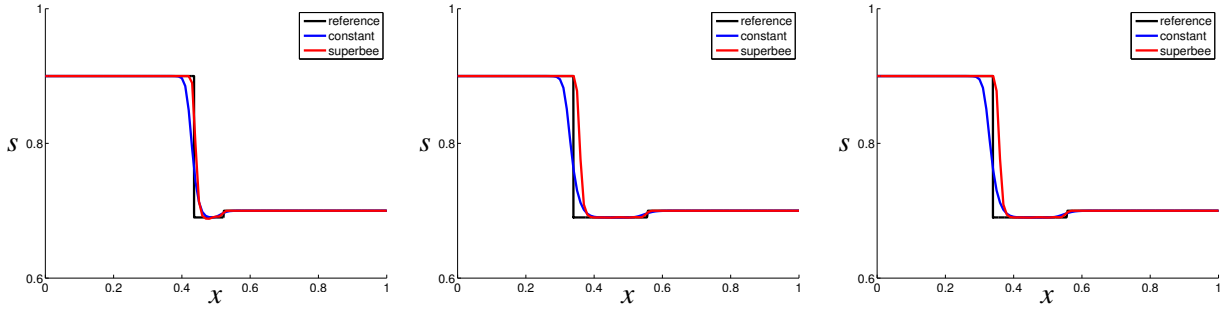

Figure 8: The saturation front at time $t = 0.2$, $t = 0.5$ and $t = 1$, from left to right, for flux shape C and initial condition (19b). Simulations from the constant reconstruction (blue) and the superbee limiter (red) compared to the reference solution (black).

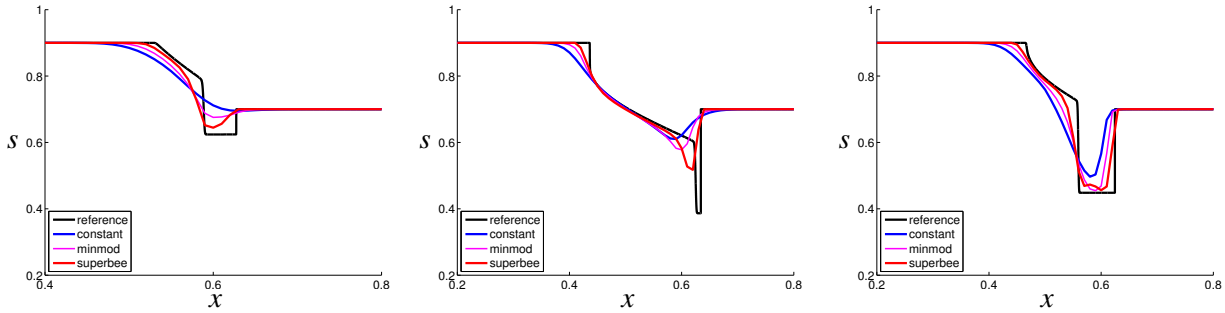

(a) (b) (c)

Figure 9: Approximations of the polymer bank in the saturation profile. Simulations from the constant reconstruction (blue), the minmod limiter (magenta), and the superbee limiter (red) compared to the reference solution (black). For the simulations in (a) the flux function is of shape A, the adsorption is taken to be of Case 2 the permeability reduction is neglected. The simulations in (b) and (c) have flux function of shape B, adsorption of Case 2 and 3, and permeability reduction of Case b and c, respectively.

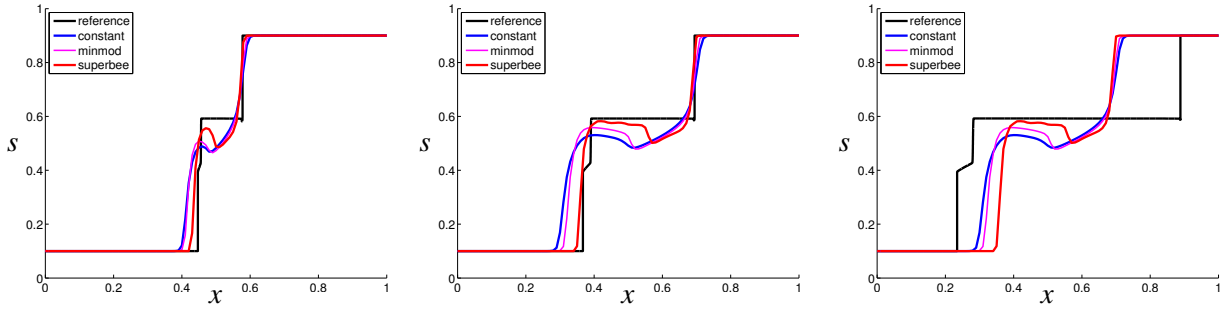

Figure 10: The saturation front at time $t = 0.2$, $t = 0.5$ and $t = 1$, from left to right, for flux shape E and initial condition (19c) with adsorption and permeability reduction neglected. Simulations from the constant reconstruction (blue), minmod limiter (magenta), and the superbee limiter (red) compared to the reference solution (black).

Table 4: Occurrence of different phenomena discussed in the text for different flux function shapes, initial conditions, adsorptions, and permeability reductions: (-) indicates no special phenomenon, (o) indicates that the oscillation in the suberbee approximation occurs, (x) indicates that the difficult oil polymer bank phenomenon are present and difficult to model, (*) indicates the false oil bank for the coarse-scale of flux D and E with initial condition (19c) - with increasing bank with increasing number of *.

Adsorption	Case	1	2			3			4			5		
Perm. red	Case	a	a	b	c	a	b	c	a	b	c	a	b	c
	Flux A	-	-	-	-	-	-	-	-	-	-	-	-	-
Initial cond. (19a)	Flux B	-	o	o	o	o	o	o	-	-	-	o	o	o
	Flux C	-	o	o	o	o	o	o	o	o	o	o	o	o
	Flux A	x	x	x	x	-	-	-	x	x	x	x	x	x
Initial cond. (19b)	Flux B	-	-	x	x	x	x	x	-	-	x	-	x	x
	Flux C	+	+	+	+	+	+	+	+	+	+	+	+	+
Initial cond. (19c)	Flux D	*	**	**	**	*	*	*	***	***	***	*	**	*
	Flux E	***	***	***	***	***	*	*	***	***	***	**	**	**

unexpected, the superbee limiter does the best job at approximating these polymer oil banks. However, also this limiter struggles, especially when the bank is narrow. In Table 4 we have summarized in which situations this oil bank occurs.

When simulating the saturation profile for flux function of shape D and E with initial condition (19c), the coarse-scale approximations introduces a false oil bank. This is shown in Figure 10 for three different times for simulations done with flux E where both adsorption and permeability reduction are neglected. In Table 4, the occurrence of this phenomenon at time $t = 0.5$ is quantified with (*), where increasing number of stars means larger oil bank for the coarse-scale simulations. One property of classical first-order, coarse-scale approximations of the contact discontinuity in polymer concentration is that it should be mass-conservative. Thus, the difference between the coarse-scale solution and a reference solution should be symmetric on both sides of the discontinuity. Since we have imposed Dirichlet boundary conditions, this is not necessarily the case. However, we should expect that solutions approximated with the same numerical scheme on different refinements of the grid should attain the same symmetry behavior.

In our numerical experiments it turns out that the error of the coarse-scale approximation of the contact discontinuity varies with how the shape of the flux function $f(s,c)$ is. Also, how the adsorption

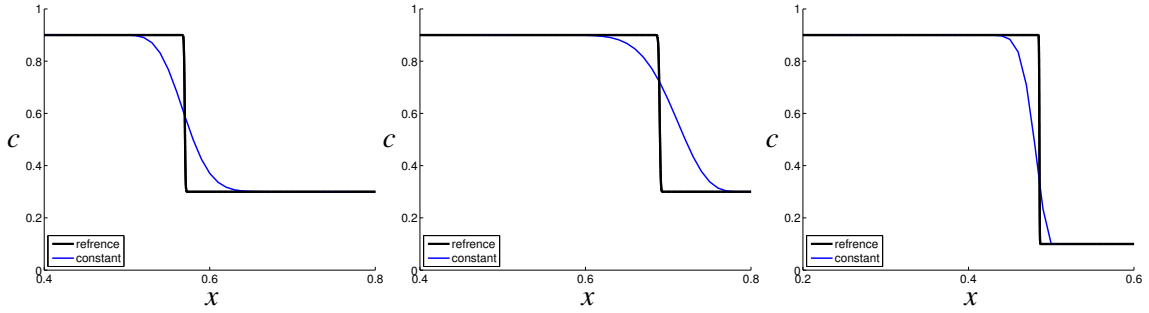

(a) $E \approx 0$. (b) $E > 0$. (c) $E < 0$.

Figure 11: Approximated polymer concentration c at time $t = 0.5$ with a coarse-scale constant reconstruction (blue) compared to a reference solution (black). Different shapes of the flux function $f(s,c)$ and adsorption term $a(c)$ create different values of E.

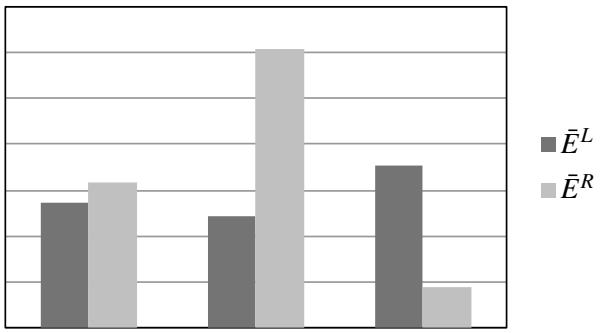

(a) $E \approx 0$ (b) $E > 0$ (c) $E < 0$

Figure 12: The bars correspond to the values $\bar{E}^L$ and $\bar{E}^R$ in dark grey and light grey respectively, for the same situations as in (a), (b) and (c) in Figure 11.

$a(c)$ and the permeability reduction $R(c)$ is modeled influences this. This means that the coarse-scale approximation can have less numerical diffusion for some examples, than for others.

We consider how the approximated polymer front from a constant reconstruction is moving compared to the reference solution. Let k be the cell index closest to the discontinuity, and define

$$\bar{E}^L = \sum_{i=1}^{k} |\bar{c}_i - c_i|, \qquad \bar{E}^R = \sum_{i=k+1}^{N} |\bar{c}_i - c_i|.$$

Thus, $\bar{E}^L$ is a measure for the error to the left of the discontinuity, and $\bar{E}^R$ as a measure of the error to the right of the discontinuity. If $E = \bar{E}^R - \bar{E}^L \approx 0$ the approximation is smeared out equally on both sides of the contact discontinuity. Also, if the propagation speed of the polymer front is overestimated, $E > 0$ and similarly $E < 0$ if the polymer front is underestimated, see Figure 11. In this figure we have compared the coarse-scale polymer front with the reference solution at time $t = 0.5$ for three different situations. The situation shown in Figure 11a is for a flux function with shape B, initial condition (19a), and adsorption Case 3. The error of the approximation is symmetrical on both sides of the discontinuity and $E \approx 0$. In Figure 11b, the only difference is that the adsorption is neglected, and here we see that the approximate polymer front moves too fast and we have $E > 0$. Finally, for the example in Figure 11c the flux function has the shape D, the initial condition (19c), and the adsorption is again Case 3. In this situation, we see that the computed polymer front moves too slow and we have $E < 0$. For the three concrete situations in Figure 11 this would correspond to the bar chart of $\bar{E}^L$ and $\bar{E}^R$ in Figure 12.

In Figure 13 and Figure 14, similar bar charts for the five different flux function shapes A-E are given for

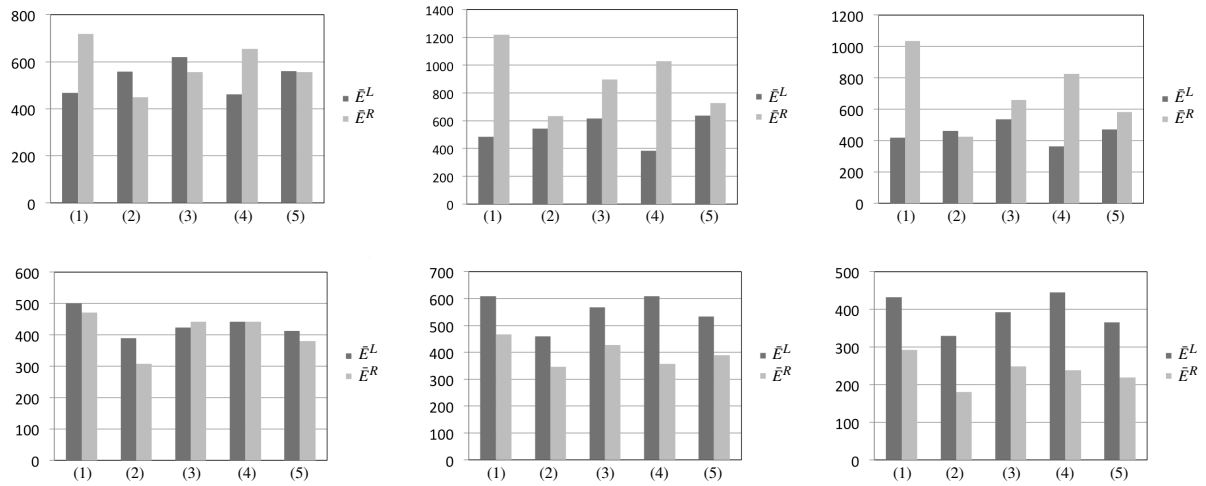

Figure 13: Six examples with $\bar{E}^L$ and $\bar{E}^R$ at time $t = 0.5$ given in dark grey and light grey, respectively, with flux functions with shapes A, B, and C, from left to right. The initial condition at the top row is (19a) and at the bottom row (19b). In each example, $\bar{E}^L$ and $\bar{E}^R$ are shown for five different adsorption situations, (1) corresponds to no adsorption, (2) is Case 3, (3) is Case 2, (4) is Case 4, and (5) is Case 5.

a variety of adsorption cases. The permeability reduction has little or no influence on this phenomeon. However, we see that depending on which adsorption function we are considering for the same flux function shape the distribution of $\bar{E}^L$ and $\bar{E}^R$ varies. For the two initial conditions (19a) and (19b) used in the examples in Figure 13, on the top and bottom row, respectively, we see that the trend is almost opposite in the two situations.

For the examples with the flux function shapes E and D in Figure 14 we see that $\bar{E}^L > \bar{E}^R$ in all cases, with varying difference.

Summary

In this work we have applied high-resolution schemes and different flux approximates to the one dimensional polymer flooding problem. Effects like adsorption and permeability reduction and different flow situations (horizontal, down and up dip) are included in the discussion. Through numerous numerical experiments we have uncovered some special numerical phenomenon of the polymer system. The central-upwind flux-approximation is compared to the two Riemann solvers based on the DFLU and the Godunov flux approximation, and found to preform similar to the Riemann solvers.

We have justified and illustrated the need of high-resolution methods and the importance of their applicability for this problem. We saw that the the superbee limiter can introduce oscillations in the saturation front, and that it can overestimate the propagation speed of the saturation front. Furthermore, we saw that polymer oil banks can be present either naturally or as a numerical byproduct for different flooding situations. These banks are especially hard to capture, and the use of accurate and valid high-resolution methods becomes important.

The coarse-scale approximations of the polymer front has varying numerical diffusion, depending on what flow we are considering and how the adsorption is modeled. This means that the propagation speed of the polymer front can be over- or underestimated, depending on what flow we are considering. Especially in two-dimensions, this can have a larger effect on the overall flow if for example the flow is horizontal in some parts and up dip in others. Therefore, this trend needs to be further investigated for the two-dimensional case.

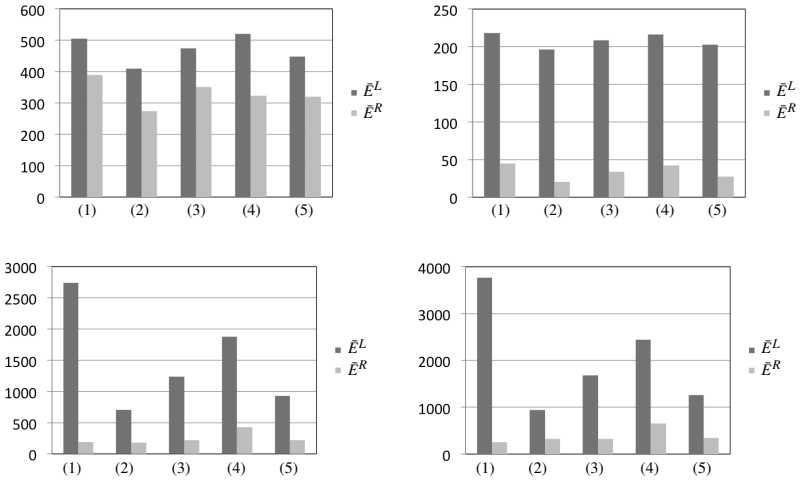

Figure 14: Four examples with $\bar{E}^L$ and $\bar{E}^R$ at time $t = 0.5$ given in dark grey and light grey, respectively, for flux functions with shapes D (left) and E (right) and initial conditions (19b) (top) and (19c) (bottom). In each example, $\bar{E}^L$ and $\bar{E}^R$ are shown for five different adsorption situations, (1) corresponds to no adsorption, (2) is Case 3, (3) is Case 2, (4) is Case 4, and (5) is Case 5.

References

Adimurthi, Jaffré, J. and Veerappa Gowda, G.D. [2004] Godunov-type methods for conservation laws with a flux function discontinuous in space. *SIAM Journal on Numerical Analysis*, **42**(1), 179–208.

Adimurthi, Veerappa Gowda, G.D. and Jaffré, J. [2013] The DFLU flux for systems of conservation laws. *Journal of Computational and Applied Mathematics*, **247**, 102–123.

Dang, C.T.Q., Chen, Z.J., Nguyen, N.T.B., Bae, W. and Phung, T.H. [2011] Development of isotherm polymer/surfactant adsorption models in chemical flooding. *Proceedings of SPE Asia Pacific Oil and Gas Conference and Exhibition, 20-22 September, Jakarta, Indonesia*, Society of Petroleum Engineers.

Hagen, T.R., Henriksen, M.O., Hjelmervik, J.M. and Lie, K.A. [2007] How to solve systems of conservation laws numerically using the graphics processor as a high-performance computational engine. In: *Geometric Modelling, Numerical Simulation, and Optimization*. 1, Springer, 211–264.

Harten, A. [1983] High resolution schemes for hyperbolic conservation laws. *Journal of Computational Physics*, **49**(3), 357–393, ISSN 00219991.

Isaacson, E.L. [1989] Global solution of a riemann problem for non-strictly hyperbolic system of conservation laws arising in enhanced oil recovery. *Rockefeller University preprints*.

Johansen, T. and Winther, R. [1988] The solution of the Riemann problem for a hyperbolic system of conservation laws modeling polymer flooding. *SIAM Journal on Mathematical Analysis*, **19**(3), 541–566.

Kurganov, A., Noelle, S. and Petrova, G. [2001] Semidiscrete central-upwind schemes for hyperbolic conservation laws and Hamilton-Jacobi equations. *SIAM Journal on Scientific Computing*, **23**(3), 707–740.

Lake, L.W. [1989] *Enhanced oil recovery*. Prentice Hall.

LeVeque, R.J. [1992] *Numerical methods for conservation laws*. Birkhauser.

Ogunberu, A. and Asghari, K. [2005] Water permeability reduction under flow-induced polymer adsorption. *Journal of Canadian Petroleum Technology*, **44**(11).

Pope, G.A. [1980] The application of fractional flow theory to enhanced oil recovery. *Society of Petroleum Engineers Journal*, **20**(3), 191–205.

Roe, P.L. [1985] Some contributions to the modelling of discontinuous flows. *Large-scale Computations in Fluid Mechanics, Proceedings of the Fifteenth Summer Seminar on Applied Mathematics,La Jolla, CA, USA, June 27 - July 8*, 163–193.

Schlumberger and Geoquest [2005] Eclipse technical description. *Multi-Segment Wells*.

Shu, C.W. [1988] Total-variation-diminishing time discretizations. *SIAM Journal on Scientific and Statistical Computing*, **9**(6), 1073–1084.

Sudarshan Kumar, K., Praveen, C. and Veerappa Gowda, G.D. [2013] Multicomponent polymer flooding in two dimensional oil reservoir simulation.

Temple, B. [1982] Global solution of the Cauchy problem for a class of 2x2 nonstrictly hyperbolic conservation laws. *Advances in Applied Mathematics*, **3**(3), 335–375, ISSN 01968858.

Todd, M.R. and Longstaff, W.J. [1972] The development, testing and applicatio of a numerical simulator for predicting miscible flood performance. *Journal of Petroleum Technology*, **24**(7), 874–882.

Van Leer, B. [1974] Towards the ultimate conservative difference scheme. II. Monotonicity and conservation

combined in a second-order scheme. *Journal of Computational Physics*, **14**(4), 361–370.
Van Leer, B. [1977] Towards the ultimate conservative difference scheme III. Upstream-centered finite-difference schemes for ideal compressible flow. *Journal of Computational Physics*, **23**(3), 263–275.
Van Leer, B. [1979] Towards the ultimate conservative difference scheme. V. A second-order sequel to Godunov's method. *Journal of Computational Physics*, **32**(1), 101–136.